Applied Physics Letters

Observation and theoretical analysis of near-infrared luminescence from CVD grown lanthanide Er doped monolayer MoS_2 triangles

Cite as: Appl. Phys. Lett. **115**, 153105 (2019); https://doi.org/10.1063/1.5120173
Submitted: 17 July 2019 • Accepted: 23 September 2019 • Published Online: 08 October 2019

Yongxin Lyu, Zehan Wu, Weng Fu Io, et al.

Applied Physics Letters ARTICLE scitation.org/journal/apl

Observation and theoretical analysis of near-infrared luminescence from CVD grown lanthanide Er doped monolayer MoS_2 triangles

Cite as: Appl. Phys. Lett. **115**, 153105 (2019); doi: 10.1063/1.5120173
Submitted: 17 July 2019 · Accepted: 23 September 2019 ·
Published Online: 8 October 2019

Yongxin Lyu, Zehan Wu, Weng Fu Io, and Jianhua Hao[a)]

AFFILIATIONS

Department of Applied Physics, The Hong Kong Polytechnic University, Hong Kong, People's Republic of China

[a)]Author to whom correspondence should be addressed: jh.hao@polyu.edu.hk

ABSTRACT

The near-infrared (NIR) emission of Er^{3+} ions has been extensively studied owing to their significance in optical communication applications. However, studies concerning the incorporation of lanthanide ions into the two-dimensional (2D) matrix are still in the early stages. In this work, we developed an ingenious two-step vapor-phase-transfer method to synthesize Er^{3+} doped MoS_2 single-crystalline monolayers. The NIR emission at 1530 nm was observed from the doped MoS_2 nanosheets under 980 nm diode laser excitation, corresponding to the energy transition from $^4I_{13/2}$ to $^4I_{11/2}$ of the Er^{3+} dopant. The concentration quenching effect was demonstrated with an optimal Er content of around 4 mol. %. To further understand the effect of lanthanide doping on the 2D MoS_2 host matrix in terms of the growth mechanism and electronic structures, theoretical analysis was performed on Er-doped monolayer MoS_2 using the density functional theory calculation. The computed band structure with the superimposed Dieke diagram was in good accordance with our experimental results. Our work offers the possibility to develop doping strategies in the 2D limit and provides an in-depth understanding of the lanthanide doping in atomically thin materials.

Investigations of two-dimensional (2D) transition metal dichalcogenides (TMDs) have received widespread attention for constructing next-generation functional devices, owing to their superior physical and chemical properties to their bulk counterparts.[1–4] Much effort has been devoted to enhancing the device performance by modulation and functionalization of pristine 2D TMDs,[5] and one of the most attracted investigations is doping engineering.[6,7] Among the dopants, lanthanide ions possess abundant energy levels in 4f orbitals to absorb and emit photons ranging from ultraviolet (UV) to infrared spectra, making them promising candidates for extending the luminescence of 2D TMD semiconductors.[8–11] In particular, the near-infrared (NIR) emission of Er^{3+} ions at 1.53 μm has been extensively studied in conventional bulk phosphors, since it is located in the "eye safe" spectral region and has promising aspects in optical communication applications.[12]

So far, the doping of 2D TMDs has been widely demonstrated by replacing the cationic atoms with transition metal dopants, such as Nb,[13,14] Mn,[15] and Re.[16] Nevertheless, doping engineering of atomically thin TMDs by introducing elements with distinct valence and atomic configurations, like lanthanide elements, remains challenging. Lanthanide source materials are hard to control during the conventional vapor phase deposition process. The pure lanthanide metals are highly unstable in the atmosphere, while the lanthanide oxides require extremely high temperature to evaporate (over 1100 °C) and their vapor pressure is too low to supply the lanthanide source.[9] In our previous work, the incorporation of Er^{3+} ions into 2D TMD nanosheets was realized using a predeposition route to deliver metal precursors,[17] which avoided the complexity of the conventional chemical vapor deposition (CVD) approach including precursor stoichiometry control and interrelated growth parameters. This two-step CVD method holds great promise for growing 2D TMD thin films on the wafer scale and was also used in other investigations.[18] In another study, the Er-doped MoS_2 film was demonstrated with a quasiclosed crucible CVD method using $ErCl_3{\cdot}6H_2O$ as the precursor and assistant agent.[32] Besides, pulsed laser deposition (PLD) was also explored to deposit Yb/Er codoped WSe_2 layers.[19] However, only polycrystalline ultrathin films with unpredictable defects were obtained in these studies, which limited further investigations on the doped semiconductor system and extensive applications in optoelectronic devices. In this work, an ingenious modification on the two-step CVD method was put forward by

designing a gas-induced-transfer process of the metal precursor to obtain Er-doped MoS_2 single crystals with a well-defined triangular shape. The luminescence of the 2D MoS_2 host was effectively extended to the NIR spectra range at 1.53 μm. Furthermore, to investigate the thermal stability and electronic structure of the doped system, first principles calculations on the Er-doped MoS_2 monolayer were demonstrated.

The general scheme for synthesis of Er-embedded MoS_2 single crystals using the two-step CVD method is presented in Fig. 1. Prior to the growth, the Mo:Er metal precursor, named as "seeds," was deposited on the substrate using magnetron sputtering. Specifically, a hard mask was covered on part of the substrate to create a reserved area for the self-assembly process of seeds. During the subsequent sulfurization process, the difference in the sulfur vapor concentration led to distinct growing schemes, as depicted in the bottom panel of Fig. 1: *in situ* sulfurization (route I) and gas phase induced transfer (route II). The insufficient sulfur concentration can be induced by low temperature of heating zone I or early introduction of carrier gas. In this case, the transformation of the Mo:Er film to the MoS_2:Er film accompanied by an increase in the thickness occurred, which is similar to previously reported studies.[13,18] By contrast, the seeds exhibited a carrier-gas-induced-transfer behavior under sulfur-rich conditions. The evaporated Mo and Er atoms from the seeds reacted with the injected high concentration sulfur vapor and were carried to the self-assembly field to form highly crystalline triangular domains with a typical lateral size of 5 μm. The structural information and chemical composition of the synthesized materials were characterized by optical microscopy, atomic force microscopy (AFM), energy dispersive X-ray spectroscopy (EDS), and X-ray photoelectron spectroscopy (XPS). AFM analysis was carried out using an Asylum MFP 3D Infinity system. EDS analysis was performed with a TESCAN VEGA3 scanning electron microscopy (SEM) system, and the XPS analysis was performed with a Thermal Scientific Nexsa system. Raman spectra and bandgap emission spectra were recorded in a WITec confocal Raman microscopic system with a 532 nm laser. The NIR PL spectra were recorded using an Edinburgh FLSP920 spectrophotometer equipped with a commercial 980 nm laser diode.

Figures 2(a) and 2(b) exhibit the optical images of undoped and Er-doped MoS_2, respectively. Both the undoped and Er-doped MoS_2 formed into clear triangular shapes, confirming the single crystalline nature of the MoS_2 host as is well-accepted by the earlier report.[20] For the doped ones, some of the MoS_2 crystals formed into different shapes with small clusters on the surface. It was reported that the nucleation and growth of TMDs are highly sensitive to the growth environment such as pressure, temperature, precursors, substrates, and other CVD parameters.[21,22] This geometry evolution can be

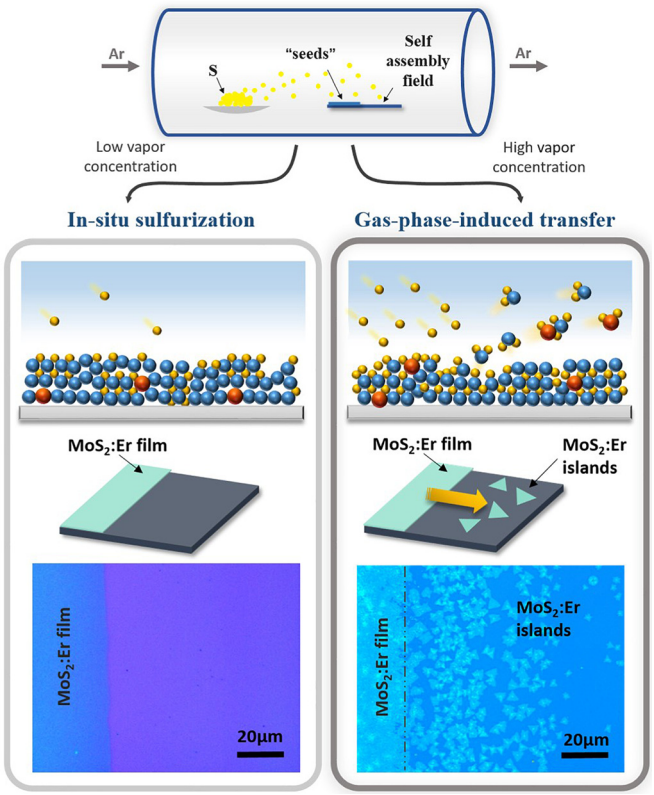

FIG. 1. Flow chart of the growth process of Er-doped MoS_2 via the two-step CVD method. The low vapor concentration (left panel) produces a large-scale polycrystalline film, while the high vapor concentration (right panel) yields discrete single crystalline islands in the self-assembly region. Blue, yellow, and red balls represent the Mo, S, and Er atoms, respectively. Scale bars: 20 μm.

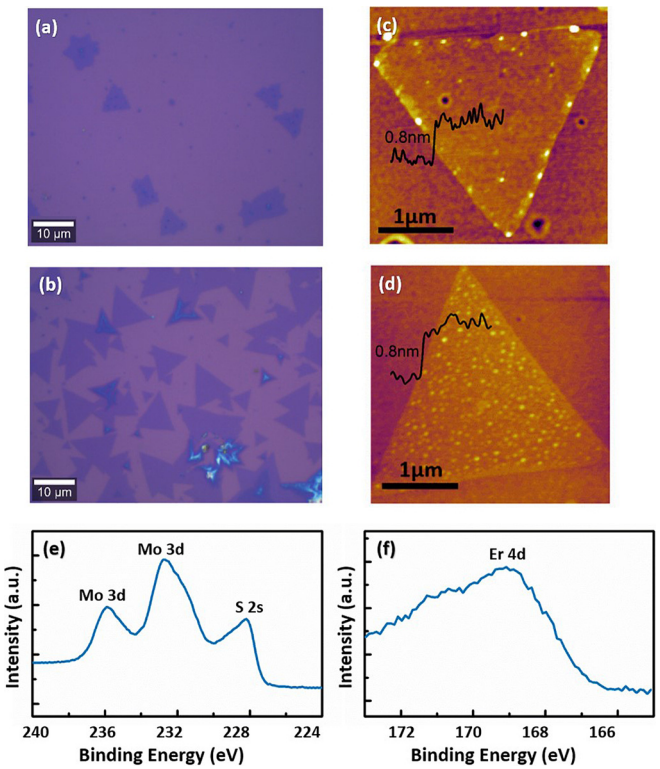

FIG. 2. Optical microscopy images of (a) Er-doped and (b) undoped MoS_2 triangles. Scale bars: 10 μm. AFM images of (c) Er-doped and (d) undoped MoS_2. Scale bars: 1 μm. XPS results of (e) Mo 3d, S 2s, and (f) Er 4d core levels of Er-doped MoS_2.

contributed to a slight change in the growth environment induced by the Er dopant. Figures 2(c) and 2(d) show the AFM image of the as-prepared pristine and doped MoS_2 samples, respectively. The height profiles indicate that the thickness of a typical flake is approximately 0.8 nm, which is almost comparable to that of the single layer MoS_2 crystal. The incorporation of the Er element is evidenced by the XPS analysis as presented in Figs. 2(e) and 2(f). It can be seen that the binding energy peaks of Er 4d core-levels at 168 eV are detected, which is consistent with the previously reported XPS feature from the $ErSi_{1.7}$ thin film.[23] Moreover, the existence of Er doping is further implied by the EDS result of Er-doped MoS_2 on the Si/SiO_2 substrate [see Fig. 3(a)], where the characteristic peaks for Mo, S, and Er elements can be recognized. The composition profile displays a relatively strong intensity of the Si element from the substrate, while the Er element exhibits a relatively weak signal due to the detection limit of EDS.

The embedding of Er atoms into the MoS_2 layer renders the possibility to investigate the optical characteristics of Er^{3+} in the 2D MoS_2 host matrix. A comparison of Raman spectra on pristine and doped MoS_2 is exhibited in Fig. 3(b), where the E^1_{2g} and A_{1g} characteristic peaks of 2H phase MoS_2 are observed at around 386 and 405 cm^{-1}, respectively. The two peaks present a frequency difference of 19.0 cm^{-1}, further evidencing the monolayer structure characterized by AFM measurements. Notably, the peak frequencies of Er-doped MoS_2 are red-shifted by 2 cm^{-1} compared with their intrinsic counterparts, which is consistent with the values in the previous report.[17] Such a Raman shift implied the incorporation of Er dopants into the MoS_2 single crystal, which can induce strain near the impurity sites and lead to slight modification of lattice vibration. To further confirm the uniformity of Er embedded into the MoS_2 lattice, Raman mapping on the intensity of E^1_{2g} and A_{1g} peaks was performed [see Figs. 3(c) and 3(d)]. The triangular regions are of high uniformity in color contrast, highly indicative of crystal quality and smoothness of the synthesized samples. Moreover, Fig. 3(e) presents the typical band-to-band emission of the MoS_2 monolayer at around 1.84 eV. The sharp excitonic A peak of Er-doped MoS_2 is slightly shifted to lower energy compared with that of undoped samples, which will be explained by computational simulation in the following discussion. The PL mapping of the bandgap emission of Er-doped MoS_2 is shown in Fig. 3(f), which is highly indicative of the consistency and uniformity of the prepared sample.

Among the Er^{3+} PL emissions, the NIR emission band at 1.53 μm is the most important one for NIR laser applications and broadband optical amplifiers at the telecommunication window. For the evaluation of spectroscopic parameters of the 1.53 μm fluorescence on 2D MoS_2 with different Er^{3+} ion concentrations, the emissions were recorded by exciting the samples with a 980 nm diode laser. The normalized spectra are presented in Fig. 4(a), in which the intense fluorescence emission peaked around 1530 nm can be clearly observed. The broad emission band consists of two peaks centered at 1529 and 1505 nm, which originate from the stark splitting induced by the surrounding chemical environment on the crystal field of Er^{3+} ions.[24,25] Figure 4(b) shows the intensity of 1.53 μm emission as a function of Er doping level in a series of samples. The PL intensity drastically increases and reaches the maximum under around 4 mol. % Er-content and then decreases with the increase in Er^{3+} concentrations. This phenomenon is referred to as concentration-quenching, which can be attributed to the increase in the nonradiative decay process favored due to the interaction between closely spaced impurities in heavily doped samples.[26] Besides, the pump power (P) dependence at

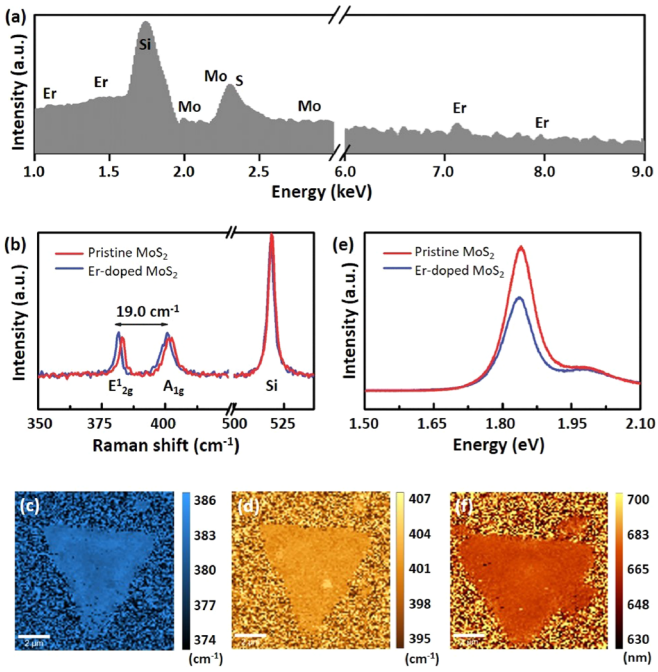

FIG. 3. (a) EDS results of Mo, S, and Er elements on Er-doped MoS_2. (b) Raman spectrum measured on pristine and Er-doped MoS_2 triangular monolayers. Raman mapping of (c) $E_{2g}{}^1$ and (d) A_{1g} peaks on Er-doped MoS_2 triangles. (e) Bandgap emission of pristine and Er-doped MoS_2. (f) PL mapping of bandgap emission of Er-doped MoS_2. Scale bars: 2 μm.

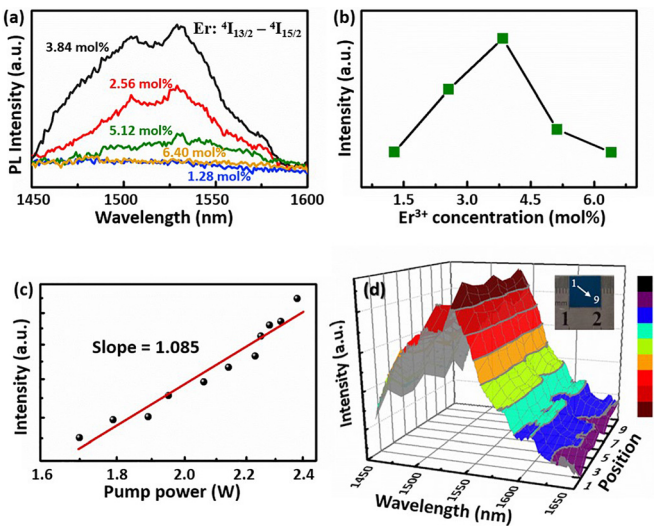

FIG. 4. (a) NIR emission at 1530 nm on MoS_2 with different Er^{3+} dopant concentrations pumped by the 980 nm laser. (b) Dopant concentration dependence of PL Intensity at 1530 nm. (c) The pump power dependence of PL intensity at 1530 nm. (d) PL spectra mapping image of the 1530 nm emission peak of nine spots in a line.

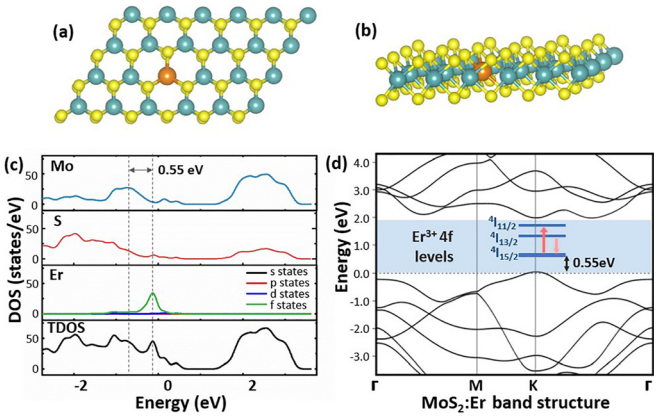

FIG. 5. (a) Top and (b) side views of the Er-doped MoS_2 supercell. Blue, yellow, and orange balls represent the Mo, S, and Er atoms, respectively. (c) Calculated DOS of the Er doped MoS_2 monolayer. (d) Schematic partial energy level diagram of the Er^{3+} ion doped in the 2D MoS_2 host.

980 nm of the luminescence intensity (I) at 1530 nm was measured. The slope is fitted to be 1.08 according to the dependence of emission intensity on the pump power as shown in Fig. 4(c), indicating that the downconversion emissions mainly originate from the one-photon process. The mapping image of the NIR PL spectra in terms of position and intensity on the Er-doped MoS_2 sample is shown in Fig. 4(d), which suggests a uniform coverage and luminescence profile of Er-doped MoS_2 on the substrate.

To provide an in-depth insight into the growth mechanism and impact of lanthanide doping on the MoS_2 host, density functional theory (DFT) calculations were performed on both pristine and Er-doped MoS_2 monolayers with the DFT+U formalism. Quantum Espresso was employed using Perdew-Burke-Ernzerhof (PBE) pseudopotentials on a $4 \times 6 \times 1$ super cell containing 72 atoms. Figures 5(a) and 5(b) exhibit the top and side views of the Er-doped MoS_2 supercell, respectively. As is shown, lanthanide doping was performed by substituting one Mo atom by one Er atom, yielding a doping content of 4.16 mol. %, which is comparable to the optimal concentration measured in our experiment. Parameters of the well relaxed crystal structures are presented in Table I, in which an outward distortion of S atoms can be observed surrounding the Er dopant sites. The Er-S bond is elongated by roughly 9.2% compared with Mo-S bonds, and the S-Er-S angle is increased by around 4.6%. Besides, the formation energy of doping E_{form} was calculated using the previously reported method as[27]

$$E_{form} = E_{doped} - E_{pristine} - \mu_{Er} + \mu_{Mo}, \quad (1)$$

where E_{doped} and $E_{pristine}$ are the total energies of doped and pristine MoS_2 supercells, respectively. μ denotes the chemical potential for various elements. The dopant chemical potential μ_{Er} can be obtained from energy of the bulk metal with a hexagonal structure. The Mo chemical potential μ_{Mo} is typically considered between the two limits, i.e., the Mo-rich (S-poor) condition where μ_{Mo} is set as the total energy of an Mo atom in the ground state Mo crystal and the S-rich condition in which μ_{Mo} can be obtained assuming the equilibrium of MoS_2 with the chalcogen source. Therefore, we define

$$\mu_{Mo}^{S-poor} = \mu_{Mo}^{0}, \quad (2)$$

$$\mu_{Mo}^{S-rich} = E_{MoS_2} - 2\mu_{S}^{0}, \quad (3)$$

where μ_{Mo}^{0} and μ_{S}^{0} are the chemical potentials taken in standard conditions and E_{MoS_2} is the energy of a perfect MoS_2 crystal per formula unit. The obtained doping energies under S-rich and S-poor conditions are 0.834 and 3.534 eV, respectively. The lower dopant substitutional energy under the S-rich condition implies that the incorporation of Er is highly favored and the doped system is more thermodynamically stable under the high S content. This result is consistent with our experimental data and has a similar trend to previous reports on DFT calculations of other lanthanide dopants.[28,29] Moreover, the density of states (DOS) of the doped MoS_2 monolayer with individual element contribution was simulated [see Fig. 5(c)]. After Er^{3+} doping, the majority of the DOS structure remains unchanged since the electronic bands are mainly composed of the host Mo and S states. The Er^{3+} impurity states give rise to the maximum of electron density distribution emerging at the edge of the valence band, resulting in a slight narrowing of the host bandgap. By taking the energy difference between the maximum of Er^{3+} 4f states (−0.12 eV) and Mo states (−0.67 eV), the location of the Er^{3+} 4f ground level in the host bandgap was estimated to be 0.55 eV. Since the DFT calculations are mainly based on "one electron" theory, it is not possible to directly simulate the multiplet splitting of the unfilled Er^{3+} 4f shells.[30] Alternatively, we predicted the energy level diagram of Er-doped MoS_2 by linking the lowest Er^{3+} 4f level with the top of the MoS_2 valence band. The location of other unfilled 4f states was deduced according to the Dieke diagram, considering that the lanthanide 4f-4f transitions are typically independent of the host matrix under the shielding of outer orbitals.[31] Figure 5(d) depicts the obtained energy level diagram with the corresponding excitation and emission path. The incorporation of Er^{3+} ions introduces extra energy states within the MoS_2 bandgap, enabling the energy transitions in the NIR spectral range. Upon 980 nm laser pumping, electrons are populated from the ground state $^4I_{15/2}$ to $^4I_{11/2}$ manifold and rapidly nonradiatively relax to the $^4I_{13/2}$ metastable level where the radiative transitions then take place. This proposed model is in good accordance with our experiment and implies that the 2D MoS_2 host is an appropriate candidate for promoting the NIR emission at 1.53 μm of the incorporated Er^{3+} ions.

In conclusion, by exploiting a two-step approach of metal precursor synthesis using the predeposited metal film as seeds, we have fabricated Er embedded MoS_2 triangle islands along the in-plane size up to around 10 μm, which is apparently formed into single crystals. Intriguingly, highly crystalline MoS_2:Er flakes are formed by high concentration sulfur vapor induced transfer in the self-assembly region. In comparison with the direct CVD methods, the proposed two step CVD method is promising for developing doped 2D TMD systems, especially for lanthanide dopants. First, our method reduces the complexity of the conventional CVD method by simplification of

TABLE I. Calculated lattice parameters of the Er doped MoS_2 monolayer.

	Atomic radius (Å)		Bond length (Å)		Angle (°)	
Pure MoS_2	Mo	1.90	Mo-S	2.40	S-Mo-S	81.07
Er: MoS_2	Er	2.26	Er-S	2.62	S-Er-S	84.82

precursor stoichiometry control and interrelated growth parameters. Besides, the employment of mixed metal seeds significantly reduces the reaction temperature to activate the lanthanide precursor. Moreover, this approach can be universalized to other lanthanide dopants or TMD hosts on arbitrary substrates since the deposition of precursors can be easily controlled by sputtering for most metal elements. Therefore, this work should pave the way for future investigation into doping and alloying of 2D materials, as well as potential development in both fundamental and promising applications.

This work was supported by a grant from the Research Grants Council (RGC) of Hong Kong (RGC GRF No. PolyU 153281/16P).

REFERENCES

[1]M. Chhowalla, H. S. Shin, G. Eda, L. J. Li, K. P. Loh, and H. Zhang, Nat. Chem. **5**, 263 (2013).
[2]G. R. Bhimanapati, Z. Lin, V. Meunier, Y. Jung, J. Cha, S. Das, D. Xiao, Y. Son, M. S. Strano, V. R. Cooper, L. Liang, S. G. Louie, E. Ringe, W. Zhou, S. S. Kim, R. R. Naik, B. G. Sumpter, H. Terrones, F. Xia, Y. Wang, J. Zhu, D. Akinwande, N. Alem, J. A. Schuller, R. E. Schaak, M. Terrones, and J. A. Robinson, ACS Nano **9**, 11509 (2015).
[3]Y. Shi, H. Li, and L. J. Li, Chem. Soc. Rev. **44**, 2744 (2015).
[4]Z. Yang, Z. Wu, Y. Lyu, and J. Hao, InfoMat **1**, 98 (2019).
[5]W. Jie, Z. Yang, F. Zhang, G. Bai, C. W. Leung, and J. Hao, ACS Nano **11**, 6950 (2017).
[6]K. Dolui, I. Rungger, C. D. Pemmaraju, and S. Sanvito, Phys. Rev. B **88**, 075420 (2013).
[7]V. P. Pham and G. Y. Yeom, Adv. Mater. **28**, 9024 (2016).
[8]X. Qin, X. Liu, W. Huang, M. Bettinelli, and X. Liu, Chem. Rev. **117**, 4488 (2017).
[9]G. Bai, M.-K. Tsang, and J. Hao, Adv. Funct. Mater. **26**, 6330 (2016).
[10]W. Jie, Z. Yang, G. Bai, and J. Hao, Adv. Opt. Mater. **6**, 1701296 (2018).
[11]Z. Wu, G. Bai, Y. Qu, D. Guo, L. Li, P. Li, J. Hao, and W. Tang, Appl. Phys. Lett. **108**, 211903 (2016).
[12]W. J. Miniscalco, J. Lightwave Technol. **9**, 234 (1991).
[13]M. R. Laskar, D. N. Nath, L. Ma, E. W. Lee, C. H. Lee, T. Kent, Z. Yang, R. Mishra, M. A. Roldan, J.-C. Idrobo, S. T. Pantelides, S. J. Pennycook, R. C. Myers, Y. Wu, and S. Rajan, Appl. Phys. Lett. **104**, 092104 (2014).
[14]J. Suh, T.-E. Park, D.-Y. Lin, D. Fu, J. Park, H. J. Jung, Y. Chen, C. Ko, C. Jang, Y. Sun, R. Sinclair, J. Chang, S. Tongay, and J. Wu, Nano Lett. **14**, 6976 (2014).
[15]K. Zhang, S. Feng, J. Wang, A. Azcatl, N. Lu, R. Addou, N. Wang, C. Zhou, J. Lerach, V. Bojan, M. J. Kim, L. Q. Chen, R. M. Wallace, M. Terrones, J. Zhu, and J. A. Robinson, Nano Lett. **15**, 6586 (2015).
[16]K. Zhang, B. M. Bersch, J. Joshi, R. Addou, C. R. Cormier, C. Zhang, K. Xu, N. C. Briggs, K. Wang, S. Subramanian, K. Cho, S. Fullerton-Shirey, R. M. Wallace, P. M. Vora, and J. A. Robinson, Adv. Funct. Mater. **28**, 1706950 (2018).
[17]G. Bai, S. Yuan, Y. Zhao, Z. Yang, S. Y. Choi, Y. Chai, S. F. Yu, S. P. Lau, and J. Hao, Adv. Mater. **28**, 7472 (2016).
[18]H. Lin, Q. Zhu, D. Shu, D. Lin, J. Xu, X. Huang, W. Shi, X. Xi, J. Wang, and L. Gao, Nat. Mater. **18**, 602 (2019).
[19]G. Bai, Z. Yang, H. Lin, W. Jie, and J. Hao, Nanoscale **10**, 9261 (2018).
[20]J. Zhou, J. Lin, X. Huang, Y. Zhou, Y. Chen, J. Xia, H. Wang, Y. Xie, H. Yu, J. Lei, D. Wu, F. Liu, Q. Fu, Q. Zeng, C. H. Hsu, C. Yang, L. Lu, T. Yu, Z. Shen, H. Lin, B. I. Yakobson, Q. Liu, K. Suenaga, G. Liu, and Z. Liu, Nature **556**, 355 (2018).
[21]A. M. van der Zande, P. Y. Huang, D. A. Chenet, T. C. Berkelbach, Y. You, G.-H. Lee, T. F. Heinz, D. R. Reichman, D. A. Muller, and J. C. Hone, Nat. Mater. **12**, 554 (2013).
[22]A. Thangaraja, S. M. Shinde, G. Kalita, and M. Tanemura, Appl. Phys. Lett. **108**, 053104 (2016).
[23]N. Guerfi, T. A. N. Tan, J. Y. Veuillen, and D. B. Lollman, Appl. Surf. Sci. **56-58**, 501 (1992).
[24]K. N. Shinde, S. J. Dhoble, H. C. Swart, and K. Park, *Phosphate Phosphors for Solid-State Lighting* (Springer-Verlag, Berlin Heidelberg, 2012), p. 41.
[25]Y. Tian, R. Xu, L. Hu, and J. Zhang, J. Opt. Soc. Am. B **28**, 1638 (2011).
[26]S. Dai, C. Yu, G. Zhou, J. Zhang, G. Wang, and L. Hu, J. Lumin. **117**, 39 (2006).
[27]H.-P. Komsa and A. V. Krasheninnikov, Phys. Rev. B **91**, 125304 (2015).
[28]C. N. M. Ouma, S. Singh, K. O. Obodo, G. O. Amolo, and A. H. Romero, Phys. Chem. Chem. Phys. **19**, 25555 (2017).
[29]A. Majid, A. Imtiaz, and M. Yoshiya, J. Appl. Phys. **120**, 142124 (2016).
[30]M. Pokhrel, G. A. Kumar, C. G. Ma, M. G. Brik, B. W. Langloss, I. N. Stanton, M. J. Therien, D. K. Sardar, and Y. Mao, J. Mater. Chem. C **3**, 11486 (2015).
[31]J. Lucas, P. Lucas, T. Le Mercier, A. Rollat, and W. Davenport, *Rare Earths* (Elsevier Inc., 2015), p. 251.
[32]Y. Yang, H. Pu, J. Di, Y. Zang, S. Zhang, and C. Chen, Scripta Mater. **152**, 64 (2018).